HHS Public Access

Author manuscript

Science. Author manuscript; available in PMC 2024 July 09.

Published in final edited form as:

Science. 2024 June 14; 384(6701): eadj4301. doi:10.1126/science.adj4301.

Metabolic inflexibility promotes mitochondrial health during liver regeneration

Xun Wang[1], **Cameron J. Menezes**[1], **Yuemeng Jia**[1,8], **Yi Xiao**[1], **Siva Sai Krishna Venigalla**[1], **Feng Cai**[1], **Meng-Hsiung Hsieh**[1], **Wen Gu**[1], **Liming Du**[1], **Jessica Sudderth**[1], **Dohun Kim**[1], **Spencer D. Shelton**[1], **Claire B. Llamas**[1], **Yu-Hsuan Lin**[1], **Min Zhu**[1], **Salma Merchant**[1], **Divya Bezwada**[1], **Sherwin Kelekar**[1], **Lauren G. Zacharias**[1], **Thomas P. Mathews**[1], **Gerta Hoxhaj**[1,2], **R. Max Wynn**[3], **Uttam K. Tambar**[3], **Ralph J. DeBerardinis**[1,2,4,5], **Hao Zhu**[1,2,4,6,7], **Prashant Mishra**[1,2,4]

[1]Children's Research Institute, University of Texas Southwestern Medical Center, Dallas, TX 75390 USA.

[2]Department of Pediatrics, University of Texas Southwestern Medical Center, Dallas, TX 75390 USA.

[3]Department of Biochemistry, University of Texas Southwestern Medical Center, Dallas, TX 75390 USA.

[4]Harold C. Simmons Comprehensive Cancer Center, University of Texas Southwestern Medical Center, Dallas, TX 75390 USA.

[5]Howard Hughes Medical Institute, University of Texas Southwestern Medical Center, Dallas, TX 75390, USA

[6]Departments of Internal Medicine, University of Texas Southwestern Medical Center, Dallas, TX 75390 USA.

[7]Center for Regenerative Science and Medicine, University of Texas Southwestern Medical Center, Dallas, TX 75390 USA.

Author contributions

X.W. conceptualized the study and contributed to methodology, validation, formal analysis, carrying out the investigation, data curation, writing the original draft and reviewing and editing the manuscript, and data visualization. C.J.M., Y.J., Y.X., S.S.K.V., F.C., M.H., and W.G. contributed to formal analysis, carrying out the investigation, and data curation. L.D., J.S., D.K., S.D.S, C.B.L., Y.L., M.Z., S.M., D.B., S.K., L.G.Z., T.P.M., G.H., R.M.W. and U.K.T. contributed to carrying out the investigation. R.J.D. provided critical resources, and contributed to methodology, formal analysis, reviewing and editing the manuscript, supervision and acquired funding. H.Z. conceptualized the study, provided critical resources, and contributed to methodology, formal analysis, data curation, and reviewing and editing the manuscript, data visualization, supervision, and acquired funding. P.M. conceptualized the study, provided critical resources, and contributed to methodology, formal analysis, data curation, writing the original draft and reviewing and editing the manuscript, data visualization, supervision, and acquired funding.

Competing Interests

R.J.D. is a founder and advisor at Atavistik Bioscience, and an advisor at Agios Pharmaceuticals, Vida Ventures, Droia Ventures and Faeth Therapeutics. H.Z. is a co-founder of Quotient Therapeutics and Jumble Therapeutics, is an advisor for Newlimit, Alnylam Pharmaceuticals, and Chroma Medicines. H.Z. receives research support from Chroma Medicines and owns stock in Ionis and Madrigal Pharmaceuticals. All other authors declare that they have no competing interests.

Data and Materials Availability

All materials are available from the authors upon reasonable request. All data are available in the main article or supplementary materials, or deposited in public databases. Next-generation sequencing datasets are deposited with the NCBI GEO (accession GSE235879, GSE236043). Custom code used for natural isotope abundance correction (49) is available at github.com/wencgu/nac and archived at https://doi.org/10.5281/zenodo.10950501

[8]Present address: Stem Cell Program, Boston Children's Hospital, Boston, MA 02115 USA; Department of Stem Cell and Regenerative Biology, Harvard University, Cambridge, MA 02138 USA.

Abstract

Mitochondria are critical for proper organ function, and mechanisms to promote mitochondrial health during regeneration would benefit tissue homeostasis. We report that during liver regeneration, proliferation is suppressed in electron transport chain (ETC)-dysfunctional hepatocytes due to an inability to generate acetyl-CoA from peripheral fatty acids via mitochondrial β-oxidation. Alternative modes for acetyl-CoA production from pyruvate or acetate are suppressed in the setting of ETC dysfunction. This metabolic inflexibility forces a dependence on ETC-functional mitochondria, and restoring acetyl-CoA production from pyruvate is sufficient to allow ETC-dysfunctional hepatocytes to proliferate. We propose that metabolic inflexibility within hepatocytes can be advantageous by limiting the expansion of ETC-dysfunctional cells.

Introduction

Mitochondrial ETC dysfunction is associated with a number of common diseases, including liver conditions that affect large portions of the human population. Severe ETC inhibition and decreased mitochondrial membrane potential have been observed in animal models of cirrhosis and NAFLD (nonalcoholic fatty liver disease), as well as patient biopsies with NASH (nonalcoholic steatohepatitis), cirrhosis, and liver failure (1-4). The precise consequences of ETC dysfunction in the mammalian liver are still under intense investigation. Recent work from our lab (5) has indicated that acute inhibition of hepatic complex I is well-tolerated in adult mice, with no measurable functional phenotypes. In contrast, inhibition of mitochondrial complex IV in hepatocytes results in fatty liver disease over weeks to months, but without survival deficits. Together, these data call into question an absolute requirement for the mitochondrial ETC in livers. However, whether ETC-deficient hepatocytes have a selective deficit relative to wild-type hepatocytes is unknown. In particular, it is not clear if the mammalian liver contains quality control mechanisms to promote mitochondrial health.

Here, we report that liver regeneration is impaired in the setting of ETC dysfunction. Through an assessment of genetic mouse models, we find that parts of the canonical mitochondrial ETC are required to promote the oxidation of peripheral fatty acids in order to generate acetyl-CoA during regeneration. In the absence of mitochondrial β-oxidation, fatty acids accumulate and induce expression of PDK4 (pyruvate dehydrogenase kinase 4), a kinase that negatively regulates the pyruvate dehydrogenase complex and shuts down acetyl-CoA generation from pyruvate. Fatty acid accumulation also suppresses expression of ACSS2 (acyl-CoA synthetase short chain family member 2) which limits the production of acetyl-CoA from acetate. This metabolic inflexibility (the inability to generate acetyl-CoA from pyruvate or acetate when fatty acid oxidation is inhibited) provides a selective force that prevents the expansion of hepatocytes with loss of ETC function. Restoring pyruvate oxidation by inhibiting PDK4 allows hepatocytes to bypass this metabolic inflexibility, thereby enabling the expansion of ETC-dysfunctional hepatocytes. Together, these data

indicate that metabolic inflexibility within ETC-dysfunctional hepatocytes can promote healthy liver regeneration.

Results

Signatures of elevated fatty acid metabolism in proliferative zones of the regenerating liver.

To investigate mitochondrial changes in vivo in the setting of liver regeneration, we used the conditional MITO-TAG allele mouse (6), which induces expression of an HA-tagged mitochondrial outer membrane protein (HA-GFP-omp25). Rapid pulldowns with anti-HA magnetic beads allow isolation of intact organelles in a highly enriched fraction, enabling organellar quantitation of mitochondrial metabolites in specific cell populations (6, 7). We coupled this allele with a number of Cre-drivers, which induced recombination in various hepatocyte populations (Figure 1A-C). Western blot analysis of purified organelles indicated high enrichment and specificity for mitochondrial proteins, with limited to no contamination from other cellular compartments (Figure S1A), consistent with previous results (6). Mice were subjected to a 70% partial hepatectomy (PHx) procedure, and plasma samples and liver mitochondria were collected at day 0 (pre-PHx) or day 2 following PHx, followed by LC-MS metabolomics (Figure 1C). We observed changes in several plasma metabolites following PHx, which were largely conserved between the different Cre lines (Figure S1B,C, Data S1). These changes included elevations in phosphoethanolamine and amino acid species, as well as depletion in free fatty acid and acyl-carnitine species (Figure S1C).

To assess changes in hepatic mitochondria during liver regeneration, we first evaluated mitochondria from all hepatocytes, using an Albumin-Cre driver (Figure 1D,E,F). We identified mitochondrial specific metabolites by comparison with pulldowns from control animals, which resulted in quantitation of 173 common metabolites in Day 0 and Day 2 samples (Data S1; Figure 1D). Unsupervised principle component analysis (PCA) reliably separated the metabolomes of Day 0 and Day 2 post PHx mitochondria, and differential analysis revealed a number of changing metabolites (Figure 1E, Data S1). An assessment of the top upregulated mitochondrial metabolites during regeneration suggested changes in ketone body, lipid, and amino acid metabolism (Figure S2A). We observed significant elevation in fatty acid oxidation products and ketone bodies [acetoacetate ($q=0.0029$), β–hydroxybutyrate ($q=0.0074$), and acetyl-CoA ($q=0.0038$)] in day 2 post PHx mitochondria (Figure 1F). Other CoA species (succinyl-CoA, propionyl-CoA) and ketogenic amino acids were not elevated, and we did not observe changes in pyruvate or most mitochondrial TCA cycle metabolites (Figure S2B).

Recent data have indicated that hepatocyte contribution to regeneration post-PHx is varied, with the largest contributions from periportal (zone 1) and mid-zonal (zone 2) hepatocytes (8, 9). We therefore made use of animals with zone-specific Cre-drivers (Figure 1A,B) to evaluate changes in mitochondrial metabolomes in day 0 and day 2 post PHx livers, using the MITO-TAG strategy described above. Prior to regeneration (day 0), the mitochondrial metabolomes were largely similar between zones (Figure S2C). However, at day 2 post PHx, mitochondrial metabolites had distinct zonal profiles which could be recognized by unsupervised analysis (Figure S2C). In particular, we observed large alterations in the

metabolomes of zone 1 and zone 2 mitochondria, with relatively smaller changes in zone 3 mitochondria (Figure 1G, Figure S2D, Data S1). Similar to bulk liver mitochondria, zone 1 and zone 2 mitochondria exhibited elevations in acetoacetate, β–hydroxybutyrate, and acetyl-CoA, as well as fatty acid oxidation intermediates (Figure 1H), with no elevations in ketogenic amino acids or TCA cycle metabolites (Figure S2E,F). Zone 3 mitochondria exhibited similar elevations in a subset of fatty acid metabolites (Figure 1H); in addition, elevations were noted in a number of mitochondrial TCA cycle metabolites (Figure S2G).

These data indicate differences between the mitochondrial metabolomes of regenerating hepatocytes compared to homeostatic hepatocytes, particularly with respect to fatty acid oxidation (FAO) products. To examine if the liver undergoes fatty acid oxidation post PHx, we infused animals via their tail vein with BSA-conjugated palmitate uniformly labeled with ^{13}C ([U-^{13}C]palmitate; Figure S3A), which resulted in ~25% labeling of free palmitate (FA 16:0) in plasma (Figure S3B, Data S2). During FAO, 2 carbon units are sequentially removed from acyl-CoA moieties as acetyl-CoA, which can then enter the TCA cycle for further oxidation or be converted to ketone bodies (Figure S3A). In infused animals, we observed decreasing labeling in 14:0, 12:0, 10:0, 8:0, 6:0, and 4:0 acyl-carnitine species in both the plasma, as well as heart and liver tissue, consistent with active FAO (Figure S3C, Data S2). Here, acyl-carnitines are used as proxy for labeling in acyl-CoAs, as these species are thought to be in fast exchange. We also observed m+2 labeling in acetyl-carnitine (2:0 carnitine) and acetyl-CoA, consistent with active FAO of fully labeled palmitate (Figure S3C,D, Data S2). Acetyl-CoA can be converted to β-hydroxybutyrate, or enter the TCA cycle resulting in m+2 labeled species, as well as m+1 labeled species (after one TCA cycle turn). We observed substantial labeling in m+2 β-hydroxybutyrate, as well as m+2 and m+1 TCA cycle intermediates (Figure S3D, S4, Data S2). As expected, we did not observe m+2 or m+3 labeling in pyruvate and lactate (glycolytic intermediates; Figure S3D, S4). These labeling patterns are all consistent with active FAO both prior to and after partial hepatectomy. In liver tissue, we observed significant enrichment increases in m+2 acetyl-CoA ($p=0.0044$), m+2 β-hydroxybutyrate ($p=0.00092$), and some m+2 TCA cycle intermediates (citrate, $p=0.00018$; succinate, $p=0.00030$; fumarate, $p=0.038$) following partial hepatectomy (Figure S3D). These data suggest that liver FAO capacity may be increased following PHx, discussed more below.

Proliferating hepatocytes require a functional mitochondrial ETC during liver regeneration.

To directly investigate a requirement for mitochondrial ETC activity during liver regeneration, we made use of mice bearing individual conditional knockout alleles for key components in complex I (*Ndufa9*), II (*Sdha*), III (*Uqcrq*), IV (*Cox10*) or V (*Atp5f1a*). We verified that knockout of each component impaired protein production and complex activity and assembly in liver tissue following administration of AAV-Cre (Figure S5A-G), consistent with previous studies using these alleles (5, 10, 11). We first infected animals with a low dose of AAV-Cre, which induced recombination in ~5% of hepatocytes (Figure 2A,B). In these experiments, we made use of a conditional reporter allele (*mitoDendra2*^{flox}) (12) to mark infected cells and follow their fate during regeneration. We observed marked expansion of wild-type and *Ndufa9*$^{-/-}$ clones at 2 weeks post PHx, with no significant differences between groups (Figure 2B,C). In contrast, we did not observe expansion of

Sdha$^{-/-}$, *Uqcrq*$^{-/-}$, *Cox10*$^{-/-}$ or *Atp5f1a*$^{-/-}$ clones (Figure 2B,C). Quantitative analysis of the total percentage of DENDRA2^{+}HNF4α^{+} hepatocytes at 2 weeks post PHx revealed a significant ($p<10^{-15}$) defect in the representation of *Sdha*$^{-/-}$, *Uqcrq*$^{-/-}$, *Cox10*$^{-/-}$ or *Atp5f1a*$^{-/-}$ hepatocytes, as compared with wild-type or *Ndufa9*$^{-/-}$ hepatocytes (Figure 2C), indicating that inhibition of complexes II, III, IV, or V, but not complex I, impairs hepatocyte proliferation during liver regeneration in a cell-autonomous manner.

To examine the effects from complete hepatic loss of mitochondrial ETC function, we used intravenous administration of AAV8 viral particles expressing GFP or Cre-recombinase (driven by the liver-specific *SERPINA7* promoter) at high doses (Figure 2D), which allows for complete knockout of target proteins in Cre-infected livers (5) (Figure S5B). Four weeks post-AAV administration, we subjected control (AAV8-GFP infected; hereafter "$^{f/f}$") and knockout (AAV8-Cre infected; hereafter "$^{-/-}$") animals to 70% partial hepatectomy. At one day post PHx, we observed expression of CCND1 (Cyclin D1) in wild-type and *Ndufa9*$^{-/-}$ livers, an early marker of hepatocyte proliferation (13, 14) (Figure S5H,I). We did not observe CCND1 expression in *Sdha*$^{-/-}$, *Uqcrq*$^{-/-}$, *Cox10*$^{-/-}$, or *Atp5f1a*$^{-/-}$ livers (Figure S5I), indicating that complexes II – V are required for hepatocyte proliferation following PHx.

Wild-type, *Ndufa9*$^{-/-}$ and *Cox10*$^{-/-}$ animals routinely survived PHx procedures, while *Sdha*$^{-/-}$, *Uqcrq*$^{-/-}$ and *Atp5f1a*$^{-/-}$ animals died between 24 and 48 hours post PHx. We evaluated livers from the surviving genotypes (*Ndufa9*$^{-/-}$, *Cox10*$^{-/-}$) to investigate the longer term consequences of ETC dysfunction during organ regeneration (Figure 2D). At two days post PHx, we observed a substantial number of BrdU^{+} cells in control and *Ndufa9*$^{-/-}$ livers, indicating that complex I is dispensable for hepatocyte proliferation (Figure S6A,B). In contrast, C*ox10*$^{-/-}$ livers exhibited a severe lack of cellular proliferation at two days post-injury, which did not substantially increase at later timepoints (Figure 2E,F). *Cox10*$^{-/-}$ livers were also deficient in mitotic hepatocytes, which were readily observed by phospho-HISTONE3 staining in control livers (Figure S6C). Histological analysis revealed substantial hepatocyte lipid accumulation and increased organ weight in *Cox10*$^{-/-}$, as compared with control and *Ndufa9*$^{-/-}$ livers (Figure 2E,G, S6D,E), without signs of necrosis or apoptosis (Figure S6F). We observed similar results in animals subjected to the hepatotoxin CCl_4 (Figure S6G), which induced a substantial number of BrdU^{+} hepatocytes at 2 days post administration in control but not *Cox10*$^{-/-}$ livers (Figure S6H-J).

Allotopic expression of alternative oxidase (AOX), an ascidian enzyme which can oxidize ubiquinone and reduce oxygen in the mitochondria (Figure S7A), confers resistance to complex IV inhibitors and complex III deficiency in cancer cells by restoring ubiquinone oxidation and oxygen consumption (15, 16). We therefore tested if expression of AOX in *Cox10*$^{-/-}$ hepatocytes is sufficient to alleviate proliferation defects during liver regeneration. *Cox10*$^{f/f}$ animals infected with AAV-Cre-IRES-AOX exhibited restored BrdU^{+} cells and decreased liver weight and fat accumulation, indicating that allotopic expression of AOX is sufficient to reverse regenerative defects in this genetic model (Figure S7B,C). Altogether, these results indicate that a functional mitochondrial ETC is required in a cell-autonomous fashion for hepatocyte proliferation in response to partial hepatectomy, and that mitochondrial complex I is dispensable for liver regeneration.

Cholangiocytes compensate and contribute to liver regeneration in the absence of mitochondrial complex IV function

Mice with hepatocyte-specific depletion of Cox10 (via AAV8-*SERPINA7*-Cre infection) uniformly survive partial hepatectomy procedures (Figure 3A). Histological analysis of livers at 2 weeks, 4 weeks, and 8 months revealed that the fat-filled hepatocytes readily observed at early timepoints (2 – 7 days post PHx, Figure 2E) are largely diluted at later timepoints (Figure 3B), suggesting that an alternative cell type may be contributing to liver regeneration. Previous reports have indicated that in the absence of hepatocyte proliferation, cholangiocytes (biliary epithelial cells (BECs)) can transdifferentiate into hepatocytes and contribute to liver regeneration (17-20). Indeed, an analysis of *Cox10*$^{-/-}$ livers at early time points revealed BrdU staining that localized near biliary structures and colocalized with CK19^{+} staining for cholangiocytes (Figure 3C; Figure S8A). In addition, immunofluorescent analysis of *Cox10*$^{-/-}$ regenerating livers at later stages revealed a substantial contribution from DENDRA2^{-} cells, representative of a non-Cre expressing cell type (Figure S8B,C).

We therefore used a *Ck19-Cre* driver, combined with a *tdTomato* reporter allele to trace the fate of cholangiocytes in wild-type and *Cox10*$^{-/-}$ livers post partial hepatectomy. In these experiments, we used Cas9-expressing mice, which were infected with AAV8 particles expressing either control or *Cox10* targeted sgRNAs in hepatocytes (Figure 3D,E). In *Cox10* targeted livers, we observed substantial expansion of tdTomato^{+} HNF4α^{+} cells, which was not observed in control livers (Figure 3F). Thus, in the absence of hepatocyte complex IV function, cholangiocytes transdifferentiate and contribute to liver regeneration. We also observed contribution of non-hepatocyte populations in *Cox10*$^{-/-}$ animals under homeostatic (no PHx) conditions at 8 months post *Cox10* deletion (Figure S8D), suggesting that transdifferentiation of BECs may play a physiological role in the setting of hepatocyte mitochondrial dysfunction.

We hypothesized that the survival of *Cox10*$^{-/-}$ animals post PHx (Figure 3A) is dependent on BEC expansion. To investigate this, we made use of an *Albumin*-Cre driver allele, combined with conditional *Cox10*^{flox} and *mitoDendra2*^{flox} alleles, which resulted in *Cox10* deletion and reporter expression in both hepatocytes and BECs (21) (Figure S8E). As before, we observed a large decrease in BrdU incorporation at day 2 post PHx (Figure 3G, Figure S8F). In contrast with mice modified by hepatocyte-specific deletion of Cox10 via AAV8-*SERPINA7*-Cre infection (Figure 2D-G), these mice (driven by Alb-Cre expression in hepatocytes and BECs) exhibited a rapid survival deficit (Figure 3H). These results indicate that transdifferentiation of BECs is required for liver regeneration in the setting of hepatocyte complex IV inhibition and critical for survival.

A recent study indicates that transdifferentiation of BECs into hepatocytes occurs by the sequential procession through TLPC (transitional liver progenitor cell) stage 1 (CK19^{+}, HNF4α^{+}) and TLPC stage 2 (CK19^{-}, HNF4α^{+}) fates prior to adopting a bona-fide hepatocyte identity (18). Single-cell analyses of regenerating livers at an early stage have captured stage 1 TLPCs, which exhibit alterations in Notch signaling to complete the transdifferentiation process (18). In contrast, little is known about the properties of stage 2 TLPCs. We reasoned that examining single-cell properties of *Cox10*$^{-/-}$ livers at a late stage of regeneration might provide an opportunity to isolate unique cell populations and

study processes related to transdifferentiation. To this end, we performed single nuclei RNA-sequencing (snRNAseq) in wild-type and *Cox10*$^{-/-}$ livers at 4 weeks post PHx (Figure 3I). Wild-type livers were largely represented by hepatocytes, with small populations representing immune, stellate, Kupffer, and endothelial cells (Figure 3I, Figure S9). In contrast, *Cox10*$^{-/-}$ livers revealed two distinct hepatocyte populations (termed KO1 and KO2), as well as enrichment of cholangiocyte and other cellular populations (Figure 3I). While the wild-type hepatocyte population exhibited gene signatures of all three hepatic zones (Figure 3J), hepatocytes from *Cox10*$^{-/-}$ livers exhibited distinct zonal signatures. Specifically, the KO1 hepatocyte population exhibited expression of all three zonal markers, while the KO2 hepatocytes were enriched in zone 2 markers (Figure 3K,L).

To interrogate the transdifferentiation process in more detail, we focused our analysis on hepatocyte and cholangiocyte populations in *Cox10*$^{-/-}$ livers, which were closely spaced in our UMAP analysis (Figure 3M). Clustering analysis revealed two populations of cholangiocytes, with properties reminiscent of stage 1 TLPCS (dark blue; *Spp1*$^{+}$, *Hnf1β*$^{+}$, *Hnf4α*$^{+}$) and stage 2 TLPCs (cyan; *Spp1*$^{-}$, *Hnf1β*$^{-}$, *Hnf4α*$^{+}$) (Figure 3N). Here, we used *Spp1* and *Hnf1β* expression as indicators of cholangiocyte identity (22, 23). Our experimental enrichment and identification of these two transdifferentiating cholangiocyte populations provided an opportunity to compare expression profiles during the transdifferentiation process. Stage 2 TLPCs also expressed Zone 2 (*Igfbp2*) and Zone 3 (*Glul*) hepatocyte identity markers, which were absent in stage 1 TPLCs (Figure 3N). We additionally performed gene ontology analysis comparing stage 1 and 2 TLPCs. The top five upregulated pathways in stage 2 TLPCs were related to fatty acid / lipid metabolism, suggesting that stage 2 TLPCs have substantially enriched proteins involved in fatty acid oxidation on their way to adopting hepatocyte fates (Figure 3O, Figure S10A). In addition, we noted elevated expression of metabolic genes *Pdk4* and *Pparα* in stage 2 versus stage 1 TLPCs (Figure S10B,C), consistent with elevated fatty acid oxidation during BEC transdifferentiation.

Oxidation of peripheral fats is stimulated during liver regeneration.

The above results indicate that ETC function is required and selected for during liver regeneration. In addition, mitochondria-specific metabolic changes during regeneration largely center on fatty acid metabolism. Transient steatosis in wild-type livers during liver regeneration has been previously observed and attributed to transit of peripheral fats to the liver (24-26), based on depletion of peripheral fat stores in animals undergoing partial hepatectomy. We verified this in wild-type mice, observing lipid accumulation in livers at 2 days post PHx, which was resolved by 4 days post PHx (Figure 4A), accompanied by specific loss of gonadal fat pad mass (Figure S11A,B,C). In comparison, *Cox10*$^{-/-}$ livers exhibited a substantial accumulation of fat which was not rapidly cleared (Figure 4A). Metabolomic measurements of free fatty acids in liver tissue confirmed that several species of fatty acids transiently accumulate in control livers, but continually accumulate in *Cox10*$^{-/-}$ livers (Figure 4B, Figure S11D).

A direct experimental validation of the source and fate of hepatic lipids during liver regeneration has not been previously performed. To address this, we made use of D_2O

(^2H_2O) administration in living animals, which efficiently labels hydrogens in fatty acid species via transfer from NADPH during fatty acid synthesis (27-29) (Figure 4C). Based on established protocols (27), we first measured lipid synthesis in animals with and without partial hepatectomy using a single injection of D_2O, followed by assessment of incorporation into hepatic lipids 5 hours later (Figure 4D). We observed labeling in hepatic lipid species between 1 and 10% in wild-type livers at baseline, and labeling was suppressed at 2 days post partial hepatectomy (Figure 4E, Data S2). In *Cox10*$^{-/-}$ livers, lipid labeling was suppressed further than in wild-type animals (Figure 4E) based on fractional enrichment of labeling. Due to the substantial changes in total fatty acid pools, we also examined isotopologue abundances for labeled species. For most fatty acid species, labeled peak abundances were suppressed in *Cox10*$^{-/-}$ livers post PHx (Figure S11E, Data S2). Together, these data indicate that fatty acid synthesis does not significantly contribute to the increased steatosis of wild-type or *Cox10*$^{-/-}$ livers following partial hepatectomy.

We then performed a long-term D_2O pulse/chase experiment to label lipids in peripheral fats, based on a previously published protocol (30). Animals were given access to D_2O labeled water ad libitum for 7 weeks, followed by a 2-week washout period, prior to partial hepatectomy (Figure 4F). During the labeling period, labeled fatty acids accumulate in both adipose and liver tissue; however, during the washout, fatty acid in the liver is rapidly turned over, while fatty acids in adipose tissue are relatively stable (30). Indeed, at the end of the 9-week pulse/chase period, we observed 10-50% labeling in adipose tissue fatty acid species, with lower levels in livers (1-10%) (Figure 4G, Day 0, Data S2). In mice subjected to partial hepatectomy, we observed increases in fatty acid species labeling in the liver at day 1 post PHx (Figure 4G, Figure S12, Data S2). In wild-type livers, labeling was decreased at day 2, suggesting rapid turnover of the fatty acid species. In contrast, labeled fatty acid species continued to accumulate in *Cox10*$^{-/-}$ livers at day 2 post PHx (Figure 4G, Figure S12). The mass isotopomer distributions of liver fatty acid species were similar to mass isotopomer distributions in the fat pads (Figure S13A,B, Data S2), consistent with peripheral fats as the major source of hepatic lipids. Thus, peripheral fats transit to the liver in response to partial hepatectomy, and their turnover is regulated by mitochondrial complex IV function.

The continued accumulation of labeled fats in *Cox10*$^{-/-}$ livers during regeneration suggests that clearance of fats is impaired in these animals. Mitochondrial fatty acid oxidation is a potential mechanism for fat clearance, which would lead to production of acetyl-CoA and ketone body species such as β−hydroxybutyrate and acetoacetate (Figure 4H), which we previously observed to be elevated in zone 1 and zone 2 mitochondria at 2 days post PHx (Figure 1). We therefore measured deuterium labeling in acetyl-CoA and β–hydroxybutyrate from control livers of mice subjected to the long term D_2O labeling experiment described above (Figure 4F), which revealed a substantial increase in labeling at 1 and 2 days post PHx (Figure 4I, Figure S14A,B, Data S2). Labeling in acetyl-CoA and β–hydroxybutyrate was largely inhibited in *Cox10*$^{-/-}$ livers, consistent with a lack of functional beta oxidation in these tissues (Figure 4I, Figure S14A,B). We verified this finding by examining the ability of primary hepatocytes to oxidize ^{14}C-labeled palmitate ex vivo (Figure S15A). As compared with wild-type hepatocytes, *Cox10*$^{-/-}$ hepatocytes had decreased FAO activity that did not increase at 2 days post-partial hepatectomy (Figure S15B). In parallel, we

observed substantial decreases in acetyl-CoA levels in *Cox10*$^{-/-}$ regenerating livers, as opposed to wild-type livers which were able to maintain and increase acetyl-CoA following PHx (Figure 4J). Acetyl-CoA has multiple fates besides energy generation, and we observed decreased histone acetylation in regenerating *Cox10*$^{-/-}$ livers, as well as decreased H3K27 marks at multiple genomic loci including key cell cycle genes (Figure S15C,D,E). These data indicate that fatty acid oxidation is a major source of acetyl-CoA for the regenerating liver, and is impaired in the setting of complex IV inhibition.

Oxidation of peripheral fatty acids promotes hepatocyte regeneration.

The above results indicate that the transit and oxidation of peripheral fatty acids is a key feature of liver regeneration. To directly test a requirement for mitochondrial fatty acid oxidation, we used Cas9-expressing mice infected with AAV8 particles expressing either control or *Hadha* targeted sgRNAs in hepatocytes. HADHA is a catalytic component of the mitochondrial trifunctional protein which regulates the oxidation of acyl-CoA species in the mitochondria (Figure 5A,B). Knockout of *Hadha* with two independent sgRNA species phenocopies *Cox10*$^{-/-}$ livers, with fat accumulation and suppressed proliferation following partial hepatectomy (Figure 5C,D). Thus, mitochondrial fatty acid oxidation is required for the proliferative hepatocyte response during tissue regeneration.

While previous studies have posited that the mobilization of peripheral fatty acids to the liver represent a requirement for efficient liver regeneration, their results indicate that hepatocyte proliferation is only partially impaired in either lipodystrophy models (31) or adipocyte-specific knockout of lipases (24). We extended these studies by evaluating the effects of acute treatment of lipase inhibitors (“ATGLi”, atglistatin and “HSLi”, NNC0076-0079) (32) starting at 8 hours prior to partial hepatectomy (Figure 5E). A serial evaluation of serum during partial hepatectomy indicates that PHx induces a rapid rise in plasma free fatty acids (FFAs), and that this is blunted by ATGLi+HSLi treatment (Figure 5E). We did not observe elevations in serum triglyceride levels during partial hepatectomy (Figure S16A). However, we did observe that hepatocytes proliferated at ~50% levels as compared with untreated animals, along with an absence of fat accumulation (Figure 5F,G). Acetyl-CoA levels were only partially diminished (Figure 5H) at day 2 post PHx. These results, combined with those of previous studies, indicate that mobilization of fatty acids from the periphery promotes, but is not absolutely required for liver regeneration.

The incongruence in phenotypes between hepatocyte deletion of *Hadha* or *Cox10* (Figure 2, Figure 5A-D) and the inhibition of lipid mobilization (Figure 5E-H) suggests that the murine liver may be able to shift to non-fatty acid sources for acetyl-CoA production under certain circumstances. Oxidation of pyruvate within the mitochondria is canonically considered to be a major potential source of acetyl-CoA (33). To investigate this, we made use of steady-state intravenous infusions of [U-^{13}C]glucose, which can create acetyl-CoA m+2 via either glycolysis or import and oxidation of lactate and pyruvate (Figure 5I). During steady state infusions performed at 2 days post PHx (Figure 5J), we observed labeling of glucose, lactate, and pyruvate in liver tissue, as well as a small amount of labeling in acetyl-CoA (Figure 5K, Figure S16B,C, Data S2). In vehicle-treated animals, acetyl-CoA m+2 labeling was <10% of pyruvate labeling (Figure 5L, Data S2), indicating that pyruvate is not a major

source of acetyl-CoA in the regenerating liver. In contrast, ATGLi/HSLi treated mice exhibit significantly ($p=1.6x10^{-4}$) higher levels of acetyl-CoA labeling, including a significantly ($p=3.8x10^{-6}$) elevated acetyl-CoA m+2 / pyruvate m+3 ratio (Figure 5K,L), indicative of elevated pyruvate dehydrogenase (PDH) contribution to acetyl-CoA. These data suggest that when peripheral transit of fatty acids is inhibited, increased pyruvate oxidation via PDH can partially compensate to promote acetyl-CoA production.

Metabolic inflexibility during mitochondrial dysfunction prevents expansion of dysfunctional clones.

In contrast with ATGL+HSL inhibition, *Cox10*$^{-/-}$ hepatocytes are unable to maintain acetyl-CoA levels (Figure 4J). We hypothesized that *Cox10*$^{-/-}$ hepatocytes might be defective in acetyl-CoA production from non-fatty acid sources, including glucose and acetate. To examine this, we performed [U-^{13}C]glucose infusions at day 2 post PHx in wild-type and *Cox10*$^{-/-}$ animals (Figure 6A,B). In contrast to ATGLi/HSLi treated animals, *Cox10*$^{-/-}$ livers did not display increases in acetyl-CoA labeling from pyruvate via PDH (Figure 6B, Figure S17A,B,C, Data S2). We additionally examined the extent to which plasma acetate might contribute to acetyl-CoA in liver following PHx. Only small changes in plasma acetate levels were observed in wild-type or *Cox10*$^{-/-}$ animals following PHx, with no significant differences in liver acetate levels between genotypes (Figure S17D,E). To examine in more depth, we performed steady-state [U-^{13}C]acetate infusions at 2 days post PHx, which revealed that *Cox10*$^{-/-}$ livers suppressed acetate conversion to acetyl-CoA relative to wild-type livers (Figure 6C,D, Figure S17F,G, Data S2). These data suggest that in the setting of complex IV dysfunction, hepatocytes are not only deficient in production of acetyl-CoA from fatty acids (Figure 4), but also suppress acetyl-CoA production from glucose/pyruvate and acetate.

To understand the mechanism underlying suppression of acetyl-CoA production from non-fatty acid sources, we evaluated expression of key enzymes in pyruvate and acetate metabolism. PDH activity (required for conversion of pyruvate to acetate) is regulated by a set of kinases (34-37) (PDK1,2,3,4), and we observed a striking elevation of PDK4 levels in *Cox10*$^{-/-}$ livers at 2 days post partial hepatectomy, which correlated with increased phosphorylation of PDH at Serine 300 (Figure 6E). We also observed suppression of ACSS1 and ACSS2 (metabolic enzymes required for synthesis of acetyl-CoA from acetate (38)) in wild-type livers post PHx. ACSS1 and ACSS2 levels were further suppressed in *Cox10*$^{-/-}$ livers (Figure 6E). We observed a similar pattern of enzyme changes in *Sdha*$^{-/-}$, *Uqcrq*$^{-/-}$ and *Atp5f1a*$^{-/-}$ livers, as well as *sgHadha* livers (Figure S17H), indicating that these changes are potentially due to defects in fatty acid oxidation. We therefore hypothesized that fatty acid accumulation in *Cox10*$^{-/-}$ livers is responsible for the induction of PDK4 and suppression of ACSS2 following partial hepatectomy. To test this, we examined livers from animals treated with ATGL and HSL inhibitors, which prevents the mobilization of peripheral fats (Figure 5). ATGLi/HSLi treatment suppressed levels of PDK4 and promoted ACSS2 expression in both wild-type and *Cox10*$^{-/-}$ livers (Figure 6F), indicating that fatty acid transfer to livers post PHx suppresses acetyl-CoA production from non-fatty acid sources. Consistent with this, we observed increased hepatocyte proliferation in *Cox10*$^{-/-}$

animals treated with ATGLi and HSLi (Figure 6G,H), supporting the model that fatty acid accumulation suppresses liver regeneration by restricting alternative routes for acetyl-CoA production in the mitochondrial and cytosolic compartments (Figure 6I).

To examine this model, we made use of treatment with dichloroacetate (DCA), a robust and bioavailable inhibitor of PDK4 (39-41), which was sufficient to ablate PDH phosphorylation at Ser300 in *Cox10*$^{-/-}$ livers (Figure 7A,B). In [U-^{13}C]glucose infused *Cox10*$^{-/-}$ animals treated with DCA, we observed significantly increased glucose contribution to acetyl-CoA as compared with vehicle-treated littermates ($p=3.9x10^{-7}$), as well as substantial increases in the acetyl-CoA m+2 / pyruvate M+3 ratio and acetyl-CoA steady state levels (Figure 7C,D, Figure S18A,B,C, Data S2). This effect was accompanied by restored proliferative capacity at 2 days post PHx (Figure 7E,F). We repeated these experiments using an alternative PDK inhibitor (PS10) with similar findings (Figure S19A-D). As these drugs inhibit multiple PDK family members, we also examined the hepatocyte response following Cas9-mediated knockout of *Cox10* and *Pdk1*, *Pdk2*, *Pdk3* or *Pdk4* (Figure 7G,H). In these experiments, control sgRNAs (sgCtrl) did not impair hepatocyte proliferation following partial hepatectomy, while sgRNAs directed against *Cox10* (sgCox10) inhibited proliferation (Figure 7G). Simultaneous expression of sgCox10 and sgRNAs targeted against *Pdk1*, *Pdk2* or *Pdk3* did not increase hepatocyte proliferation (Figure S19E). However, simultaneous expression of sgRNAs targeting *Pdk4* (sgPdk4#1 or sgPdk4#2) with sgCox10 restored hepatocyte proliferation (Figure 7I,J). These results indicate that removal of PDK4 activity in *Cox10*$^{-/-}$ livers is sufficient to promote hepatocyte proliferation despite continue mitochondrial ETC dysfunction.

These results suggest a model whereby inhibited fatty acid oxidation due to ETC dysfunction in hepatocytes results in suppression of metabolic flexibility. In principle, suppressed metabolic flexibility may be a mechanism to prevent the expansion of clones with inhibited mitochondrial function. Specifically, accumulating fatty acids in the setting of mitochondrial ETC dysfunction cell-autonomously induce PDK4 and repress ACSS2 thereby limiting metabolic flexibility in these cells (Figure 6I). To test this, we deleted ETC components of complexes II, III, IV or V in ~5% of hepatocytes by low dose administration of AAV-Cre (similar to Figure 2A-C), and examined the effect of systemic PDK4 inhibition on clone expansion during liver regeneration (Figure 7K). In vehicle-treated animals, mutant clones did not expand and were diluted by regenerating hepatocytes as before (Figure S19F). In DCA or PS10 treated animals, mutant clones were able to expand and contributed to the regenerating liver (Figure 7L,M, Figure S19G-I). These results indicate that decreased metabolic flexibility is a mechanism to prevent the expansion of ETC-dysfunctional hepatocytes.

Discussion

We found that excess hepatic fatty acid in the setting of mitochondrial dysfunction suppresses acetyl-CoA generation from non-fatty acid sources. These findings mirror early studies reflective of the Randle cycle whereby fasting or high fat meals inhibit glucose oxidation in muscle tissues (42). In the liver, metabolic inflexibility from PDK4 expression and ACSS2 suppression effectively prevents hepatocytes with mitochondrial ETC

dysfunction from shifting to an alternative source of acetyl-CoA generation in either the mitochondrial or cytosolic compartments. This effect constitutes a mechanism to select for cells with intact mitochondrial ETCs. Thus, we propose a model whereby regenerating cells use metabolic inflexibility in order to promote proliferation of healthy cells. In liver regeneration, this selection is specific to non-complex I components of the ETC, as complex I activity does not significantly impact fatty acid metabolism (5).

In the setting of hepatocyte ETC dysfunction, BECs can transdifferentiate and compensate for inhibited hepatocyte proliferation. In the above experiments, BEC contribution is critical to regeneration and survival, thereby providing evidence for the importance of BEC transdifferentiation in liver physiology. The role of BEC transdifferentiation has grown in importance as recent work (18) has found evidence for TLPCs in human samples. Our analysis of stage 2 TLPCs indicate that they upregulate fatty acid metabolism, as well as PDK4, suggesting a strong selection for mitochondrial functional cells even during the transdifferentiation process. We observed that BECs also contribute to the *Cox10*$^{-/-}$ livers under homeostatic conditions, suggesting that this phenomenon can occur in the absence of strong regenerative cues. We also found that BEC contribution shifted the zone specific composition of the liver, and it will therefore be important to address how this process might impact liver physiology.

Of note, mitochondrial ETC function is not absolutely required for cellular proliferation: When cultured with pyruvate and uridine, cells without mitochondrial genomes can adapt to loss of mitochondrial function by upregulating glycolytic processes to maintain ATP production and redox balance (43, 44). This metabolic flexibility allows cells to survive in a variety of nutrient sources, and metabolic flexibility in mammals has been attributed to an ability to survive a number of metabolic challenges, including fasting/feeding, prolonged starvation, exercise, and altered diets. Conversely, metabolic inflexibility is often considered a consequence of dysregulated metabolism and is associated with a number of disease processes (45-47). We found that promoting flexibility via PDK4 inhibition may have detrimental consequences by allowing ETC dysfunctional cells to proliferate. This finding suggests that regimens which enhance metabolic flexibility may potentially promote mitochondrial dysfunction, and thereby impact tissue health.

Materials and methods summary

Partial hepatectomy experiments in mice

Adult mice (8-10 weeks of age) were subjected to 70% partial hepatectomy under anesthesia by surgical removal of the left lateral and median lobes. For mice with conditional alleles targeting mitochondrial components, animals were administered AAV8 viruses expressing Cre recombinase or GFP under control of the hepatocyte-specific *SERPINA7* promoter via retro-orbital vein injection. Animals were euthanized between 0 and 8 months post partial hepatectomy, and tissue was collected for analysis.

Mitochondrial metabolome analysis in MITO-TAG mouse livers

Mice with hepatocyte-specific Cre alleles were combined with the conditional LSL-HA-eGFP-OMP25 to allow restricted expression of the MITO-TAG in hepatocyte populations. For zone-specific expression, Cre recombinase activity was induced by tamoxifen injection. To isolate mitochondria, ~50 mg of liver tissue was rapidly homogenized and clarified by centrifugation, followed by incubation with αHA magnetic beads. Metabolites were isolated from washed beads by incubation in acetonitrile/water (80:20 v/v), and analyzed on a Thermo Scientific QExactive HF-X hybrid quadrupole Orbitrap High-resolution mass spectrometer.

Single nucleus RNA sequencing from mouse liver.

Hepatocytes were isolated by liver perfusion from euthanized mice, followed by single nuclear isolation. Single-nucleus 3'RNA-seq libraries were prepared using a 10xGenomics Chromium Controller, and sequenced on an Illumina NextSeq500 Instrument. Downstream analyses were performed using the R package Seurat V4.3.0. Automated cell type identification was performed using the R package ScType.

Isotope tracing analysis in mice

Mice received a number of isotope tracers, including D_2O (intraperitoneal injection or 8% D_2O in drinking water) or [U-^{13}C]acetate, [U-^{13}C]glucose, or [U-^{13}C]palmitate (intravenous infusions via tail vein). [U-^{13}C]palmitate was conjugated to fatty acid-free BSA prior to infusion. Tissues were immediately frozen at the end of the infusion. For analysis, metabolites were extracted from homogenized tissue in acetonitrile/water (80:20 v/v). Metabolites were analyzed on high-resolution mass spectrometers coupled with HPLC instruments. Natural isotope abundances were corrected for ^{13}C, ^{2}H and ^{34}S manually or using the AccuCor algorithm (48, 49).

Supplementary Material

Refer to Web version on PubMed Central for supplementary material.

Acknowledgements

We thank the Moody Foundation Flow Cytometry Facility, Children's Research Institute Next Generation Sequencing Facility, Children's Research Institute Metabolomics Facility, UT Southwestern Live Cell Imaging Facility, UT Southwestern BioHPC supercomputing facility, UT Southwestern Histo Pathology Core, UT Southwestern Metabolic Phenotyping Core, Children's Research Institute Mouse Genome Engineering Facility, UT Southwestern ISC-Transgenic Core and Simmon's Cancer Center Tissue Management Shared Resource for assistance with experiments. We thank Marc K. Hellerstein (UC Berkeley), Michalis Agathocleous (UT Southwestern) and members of the Mishra, Zhu, and DeBerardinis laboratories for helpful discussions and suggestions during this project. Figures 1-3, 5-7, S3, S5, S6, S15, S17-19 were made with the help of BioRender.

Funding

This work was supported by funding from the National Institutes of Health (1DP2ES030449 and 1R01AR073217 to P.M., 1F30CA254150 to S.K., 1F31CA239330, T32GM008203 and TL1TR001104 to D.B., 1R01AA028791 and 1R01DK125396 to H.Z., R35CA22044901 and 2P50CA070907-21A1 to R.J.D., K99CA277576 to Y.X., 1R01DK62306 to R.M.W., 1F30DK137407 to C.J.M., P30 CA142543 to Simmon's Cancer Center Tissue Management Shared Resource), the Moody Medical Research Institute (research grant to P.M.), the National Science Foundation (Graduate Research Fellowships Program award 2019281210 to S.D.S.) and Human Frontier Science Program (Postdoctoral Fellowship award LT0018/2022-L to Y.X.). H.Z. was supported by the Pollack

Foundation, Simmons Comprehensive Cancer Center Cancer & Obesity Translational Pilot Award and the Emerging Leader Award from the Mark Foundation For Cancer Research (#21-003-ELA). The funders had no role in study design, data collection and analysis, decision to publish, or preparation of the manuscript.

References and notes

1. Koliaki C. et al. , Adaptation of hepatic mitochondrial function in humans with non-alcoholic fatty liver is lost in steatohepatitis. Cell Metab 21, 739–746 (2015). [PubMed: 25955209]
2. Perez-Carreras M. et al. , Defective hepatic mitochondrial respiratory chain in patients with nonalcoholic steatohepatitis. Hepatology 38, 999–1007 (2003). [PubMed: 14512887]
3. Cortez-Pinto H. et al. , Alterations in liver ATP homeostasis in human nonalcoholic steatohepatitis: a pilot study. JAMA 282, 1659–1664 (1999). [PubMed: 10553793]
4. Fromenty B, Roden M, Mitochondrial alterations in fatty liver diseases. J Hepatol 78, 415–429 (2023). [PubMed: 36209983]
5. Lesner NP et al. , Differential requirements for mitochondrial electron transport chain components in the adult murine liver. Elife 11, (2022).
6. Bayraktar EC et al. , MITO-Tag Mice enable rapid isolation and multimodal profiling of mitochondria from specific cell types in vivo. Proc Natl Acad Sci U S A 116, 303–312 (2019). [PubMed: 30541894]
7. Chen WW, Freinkman E, Wang T, Birsoy K, Sabatini DM, Absolute Quantification of Matrix Metabolites Reveals the Dynamics of Mitochondrial Metabolism. Cell 166, 1324–1337 e1311 (2016). [PubMed: 27565352]
8. He L. et al. , Proliferation tracing reveals regional hepatocyte generation in liver homeostasis and repair. Science 371, (2021).
9. Lin YH et al. , IGFBP2 expressing midlobular hepatocytes preferentially contribute to liver homeostasis and regeneration. Cell Stem Cell 30, 665–676 e664 (2023). [PubMed: 37146585]
10. Wang X. et al. , Scinderin promotes fusion of electron transport chain dysfunctional muscle stem cells with myofibers. Nat Aging 2, 155–169 (2022). [PubMed: 35342888]
11. Diaz F, Thomas CK, Garcia S, Hernandez D, Moraes CT, Mice lacking COX10 in skeletal muscle recapitulate the phenotype of progressive mitochondrial myopathies associated with cytochrome c oxidase deficiency. Hum Mol Genet 14, 2737–2748 (2005). [PubMed: 16103131]
12. Pham AH, McCaffery JM, Chan DC, Mouse lines with photo-activatable mitochondria to study mitochondrial dynamics. Genesis 50, 833–843 (2012). [PubMed: 22821887]
13. Yano K. et al. , Spatiotemporal expression of HMGB2 regulates cell proliferation and hepatocyte size during liver regeneration. Sci Rep 12, 11962 (2022). [PubMed: 35831365]
14. Bai H. et al. , Mitochondria-derived H(2)O(2) triggers liver regeneration via FoxO3a signaling pathway after partial hepatectomy in mice. Cell Death Dis 14, 216 (2023). [PubMed: 36977674]
15. Martinez-Reyes I. et al. , Mitochondrial ubiquinol oxidation is necessary for tumour growth. Nature 585, 288–292 (2020). [PubMed: 32641834]
16. Hakkaart GA, Dassa EP, Jacobs HT, Rustin P, Allotopic expression of a mitochondrial alternative oxidase confers cyanide resistance to human cell respiration. EMBO Rep 7, 341–345 (2006). [PubMed: 16322757]
17. Deng X. et al. , Chronic Liver Injury Induces Conversion of Biliary Epithelial Cells into Hepatocytes. Cell Stem Cell 23, 114–122 e113 (2018). [PubMed: 29937200]
18. Pu W. et al. , Bipotent transitional liver progenitor cells contribute to liver regeneration. Nat Genet 55, 651–664 (2023). [PubMed: 36914834]
19. Raven A. et al. , Cholangiocytes act as facultative liver stem cells during impaired hepatocyte regeneration. Nature 547, 350–354 (2017). [PubMed: 28700576]
20. Oderberg IM, Goessling W, Biliary epithelial cells are facultative liver stem cells during liver regeneration in adult zebrafish. JCI Insight 8, (2023).
21. Lin F. et al. , Detection of Albumin Expression by RNA In Situ Hybridization Is a Sensitive and Specific Method for Identification of Hepatocellular Carcinomas and Intrahepatic Cholangiocarcinomas. Am J Clin Pathol 150, 58–64 (2018). [PubMed: 29746696]

22. Pritchett J. et al. , Osteopontin is a novel downstream target of SOX9 with diagnostic implications for progression of liver fibrosis in humans. Hepatology 56, 1108–1116 (2012). [PubMed: 22488688]
23. Coffinier C. et al. , Bile system morphogenesis defects and liver dysfunction upon targeted deletion of HNF1beta. Development 129, 1829–1838 (2002). [PubMed: 11934849]
24. Chen Y. et al. , Acute liver steatosis translationally controls the epigenetic regulator MIER1 to promote liver regeneration in a study with male mice. Nat Commun 14, 1521 (2023). [PubMed: 36934083]
25. Glende EA Jr., Morgan WS, Alteration in liver lipid and lipid fatty acid composition after partial hepatectomy in the rat. Exp Mol Pathol 8, 190–200 (1968). [PubMed: 4296682]
26. Newberry EP et al. , Altered hepatic triglyceride content after partial hepatectomy without impaired liver regeneration in multiple murine genetic models. Hepatology 48, 1097–1105 (2008). [PubMed: 18697204]
27. Gosis BS et al. , Inhibition of nonalcoholic fatty liver disease in mice by selective inhibition of mTORC1. Science 376, eabf8271 (2022). [PubMed: 35420934]
28. Lewis CA et al. , Tracing compartmentalized NADPH metabolism in the cytosol and mitochondria of mammalian cells. Mol Cell 55, 253–263 (2014). [PubMed: 24882210]
29. Chen L. et al. , NADPH production by the oxidative pentose-phosphate pathway supports folate metabolism. Nat Metab 1, 404–415 (2019). [PubMed: 31058257]
30. Ward CP et al. , ER Unfolded Protein Response in Liver In Vivo Is Characterized by Reduced, Not Increased, De Novo Lipogenesis and Cholesterol Synthesis Rates with Uptake of Fatty Acids from Adipose Tissue: Integrated Gene Expression, Translation Rates and Metabolic Fluxes. International journal of molecular sciences 23, (2022).
31. Gazit V. et al. , Liver regeneration is impaired in lipodystrophic fatty liver dystrophy mice. Hepatology 52, 2109–2117 (2010). [PubMed: 20967828]
32. Mayer N. et al. , Development of small-molecule inhibitors targeting adipose triglyceride lipase. Nat Chem Biol 9, 785–787 (2013). [PubMed: 24096302]
33. Jankowska-Kulawy A, Klimaszewska-Lata J, Gul-Hinc S, Ronowska A, Szutowicz A, Metabolic and Cellular Compartments of Acetyl-CoA in the Healthy and Diseased Brain. Int J Mol Sci 23, (2022).
34. Linn TC, Pettit FH, Reed LJ, Alpha-keto acid dehydrogenase complexes. X. Regulation of the activity of the pyruvate dehydrogenase complex from beef kidney mitochondria by phosphorylation and dephosphorylation. Proc Natl Acad Sci U S A 62, 234–241 (1969). [PubMed: 4306045]
35. Popov KM et al. , Primary structure of pyruvate dehydrogenase kinase establishes a new family of eukaryotic protein kinases. J Biol Chem 268, 26602–26606 (1993). [PubMed: 8253790]
36. Popov KM, Kedishvili NY, Zhao Y, Gudi R, Harris RA, Molecular cloning of the p45 subunit of pyruvate dehydrogenase kinase. J Biol Chem 269, 29720–29724 (1994). [PubMed: 7961963]
37. Popov KM, Zhao Y, Shimomura Y, Kuntz MJ, Harris RA, Branched-chain alpha-ketoacid dehydrogenase kinase. Molecular cloning, expression, and sequence similarity with histidine protein kinases. J Biol Chem 267, 13127–13130 (1992). [PubMed: 1377677]
38. Luong A, Hannah VC, Brown MS, Goldstein JL, Molecular characterization of human acetyl-CoA synthetase, an enzyme regulated by sterol regulatory element-binding proteins. J Biol Chem 275, 26458–26466 (2000). [PubMed: 10843999]
39. Cardoso AC et al. , Mitochondrial Substrate Utilization Regulates Cardiomyocyte Cell Cycle Progression. Nat Metab 2, 167–178 (2020). [PubMed: 32617517]
40. Stacpoole PW et al. , Evaluation of long-term treatment of children with congenital lactic acidosis with dichloroacetate. Pediatrics 121, e1223–1228 (2008). [PubMed: 18411236]
41. Morten KJ, Beattie P, Brown GK, Matthews PM, Dichloroacetate stabilizes the mutant E1alpha subunit in pyruvate dehydrogenase deficiency. Neurology 53, 612–616 (1999). [PubMed: 10449128]
42. Randle PJ, Fuel selection in animals. Biochem Soc Trans 14, 799–806 (1986). [PubMed: 3536635]
43. King MP, Attardi G, Human cells lacking mtDNA: repopulation with exogenous mitochondria by complementation. Science 246, 500–503 (1989). [PubMed: 2814477]

44. Kukat A. et al. , Generation of rho0 cells utilizing a mitochondrially targeted restriction endonuclease and comparative analyses. Nucleic Acids Res 36, e44 (2008). [PubMed: 18353857]
45. Kelley DE, Goodpaster B, Wing RR, Simoneau JA, Skeletal muscle fatty acid metabolism in association with insulin resistance, obesity, and weight loss. Am J Physiol 277, E1130–1141 (1999). [PubMed: 10600804]
46. Muoio DM, Metabolic inflexibility: when mitochondrial indecision leads to metabolic gridlock. Cell 159, 1253–1262 (2014). [PubMed: 25480291]
47. Goodpaster BH, Sparks LM, Metabolic Flexibility in Health and Disease. Cell Metab 25, 1027–1036 (2017). [PubMed: 28467922]
48. Su X, Lu W, Rabinowitz JD, Metabolite Spectral Accuracy on Orbitraps. Anal Chem 89, 5940–5948 (2017). [PubMed: 28471646]
49. A customized R script for natural isotope abundance correction, 10.5281/zenodo.10950501, 2024.
50. Weinberg SE et al. , Mitochondrial complex III is essential for suppressive function of regulatory T cells. Nature 565, 495–499 (2019). [PubMed: 30626970]
51. Wei Y. et al. , Liver homeostasis is maintained by midlobular zone 2 hepatocytes. Science 371, (2021).
52. Miura H, Quadros RM, Gurumurthy CB, Ohtsuka M, Easi-CRISPR for creating knock-in and conditional knockout mouse models using long ssDNA donors. Nature protocols 13, 195–215 (2018). [PubMed: 29266098]
53. Wu CY et al. , A novel inhibitor of pyruvate dehydrogenase kinase stimulates myocardial carbohydrate oxidation in diet-induced obesity. J Biol Chem 293, 9604–9613 (2018). [PubMed: 29739849]
54. Tso SC et al. , Structure-guided development of specific pyruvate dehydrogenase kinase inhibitors targeting the ATP-binding pocket. J Biol Chem 289, 4432–4443 (2014). [PubMed: 24356970]
55. Wu CY et al. , Targeting hepatic pyruvate dehydrogenase kinases restores insulin signaling and mitigates ChREBP-mediated lipogenesis in diet-induced obese mice. Mol Metab 12, 12–24 (2018). [PubMed: 29656110]
56. Jia Y. et al. , In vivo CRISPR screening identifies BAZ2 chromatin remodelers as druggable regulators of mammalian liver regeneration. Cell Stem Cell 29, 372–385 e378 (2022). [PubMed: 35090595]
57. Wang Z. et al. , Positive selection of somatically mutated clones identifies adaptive pathways in metabolic liver disease. Cell 186, 1968–1984 e1920 (2023). [PubMed: 37040760]
58. Mitchell C, Willenbring H, A reproducible and well-tolerated method for 2/3 partial hepatectomy in mice. Nature protocols 3, 1167–1170 (2008). [PubMed: 18600221]
59. Rogers GW et al. , High throughput microplate respiratory measurements using minimal quantities of isolated mitochondria. PLoS One 6, e21746 (2011). [PubMed: 21799747]
60. Jha P, Wang X, Auwerx J, Analysis of Mitochondrial Respiratory Chain Supercomplexes Using Blue Native Polyacrylamide Gel Electrophoresis (BN-PAGE). Curr Protoc Mouse Biol 6, 1–14 (2016). [PubMed: 26928661]
61. Pachnis P. et al. , In vivo isotope tracing reveals a requirement for the electron transport chain in glucose and glutamine metabolism by tumors. Sci Adv 8, eabn9550 (2022). [PubMed: 36044570]
62. Tasdogan A. et al. , Metabolic heterogeneity confers differences in melanoma metastatic potential. Nature 577, 115–120 (2020). [PubMed: 31853067]
63. Aurora AB et al. , Loss of glucose 6-phosphate dehydrogenase function increases oxidative stress and glutaminolysis in metastasizing melanoma cells. Proc Natl Acad Sci U S A 119, (2022).
64. Chen Z. et al. , Lactate metabolism is essential in early-onset mitochondrial myopathy. Sci Adv 9, eadd3216 (2023). [PubMed: 36598990]
65. Hui S. et al. , Quantitative Fluxomics of Circulating Metabolites. Cell Metab 32, 676–688 e674 (2020). [PubMed: 32791100]
66. Mashimo T. et al. , Acetate is a bioenergetic substrate for human glioblastoma and brain metastases. Cell 159, 1603–1614 (2014). [PubMed: 25525878]
67. Zhang X. et al. , Isotope tracing reveals distinct substrate preference in murine melanoma subtypes with differing anti-tumor immunity. Cancer Metab 10, 21 (2022). [PubMed: 36457136]

68. Tumanov S, Bulusu V, Gottlieb E, Kamphorst JJ, A rapid method for quantifying free and bound acetate based on alkylation and GC-MS analysis. Cancer Metab 4, 17 (2016). [PubMed: 27594997]
69. Chambers MC et al. , A cross-platform toolkit for mass spectrometry and proteomics. Nat Biotechnol 30, 918–920 (2012). [PubMed: 23051804]
70. Agrawal S. et al. , El-MAVEN: A Fast, Robust, and User-Friendly Mass Spectrometry Data Processing Engine for Metabolomics. Methods Mol Biol 1978, 301–321 (2019). [PubMed: 31119671]
71. Rampler E. et al. , A Novel Lipidomics Workflow for Improved Human Plasma Identification and Quantification Using RPLC-MSn Methods and Isotope Dilution Strategies. Anal Chem 90, 6494–6501 (2018). [PubMed: 29708737]
72. Bowden JA, Heckert A, Ulmer CZ, Jones CM, (2017).
73. Wang X. et al. , A Mitofusin 2 - Hif1alpha axis sets a maturation checkpoint in regenerating skeletal muscle. J Clin Invest, (2022).
74. Li H, Durbin R, Fast and accurate short read alignment with Burrows-Wheeler transform. Bioinformatics 25, 1754–1760 (2009). [PubMed: 19451168]
75. Zhang Y. et al. , Model-based analysis of ChIP-Seq (MACS). Genome Biol 9, R137 (2008). [PubMed: 18798982]
76. Hao Y. et al. , Integrated analysis of multimodal single-cell data. Cell 184, 3573–3587.e3529 (2021). [PubMed: 34062119]
77. Ianevski A, Giri AK, Aittokallio T, Fully-automated and ultra-fast cell-type identification using specific marker combinations from single-cell transcriptomic data. Nat Commun 13, 1246 (2022). [PubMed: 35273156]

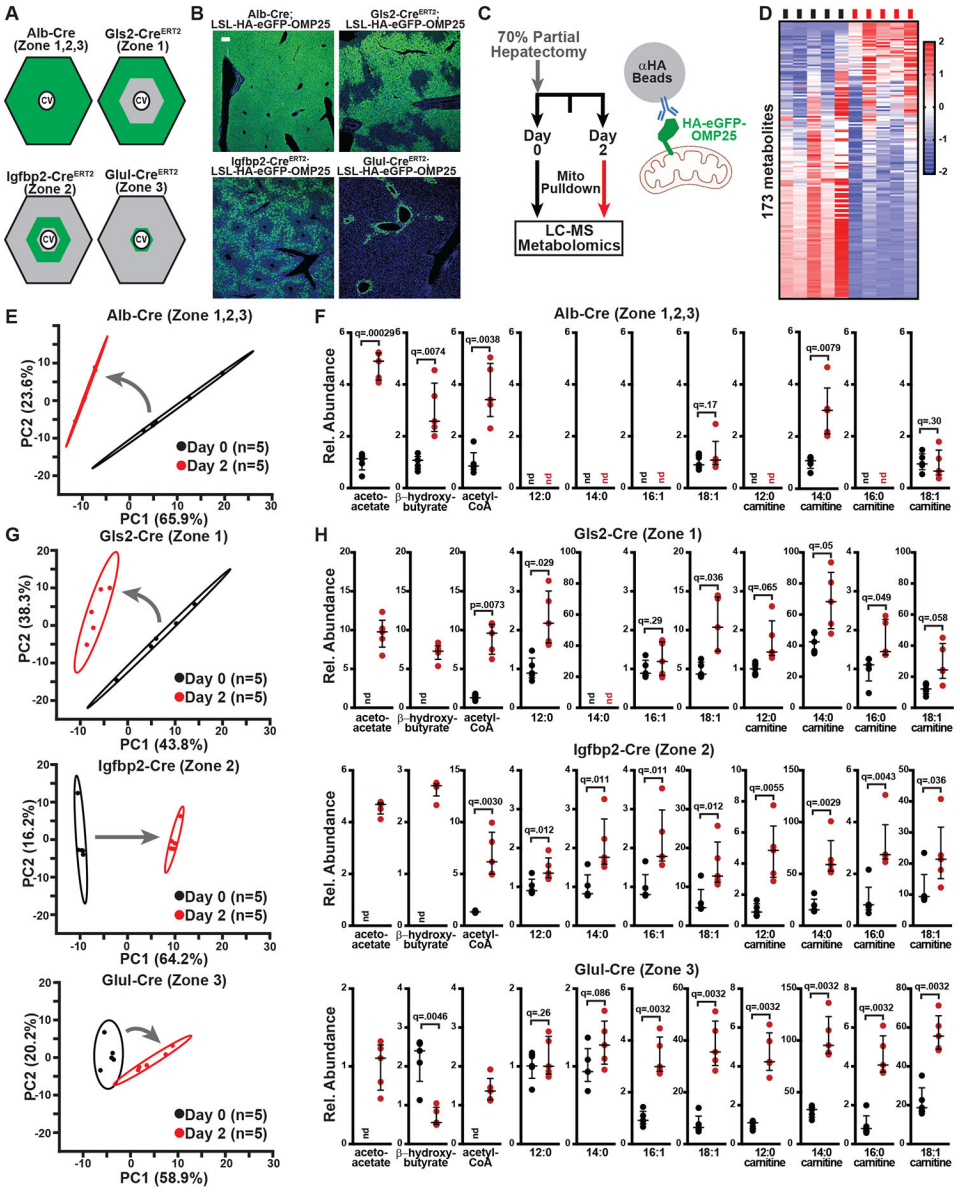

Figure 1. Zone-specific mitochondrial metabolomics in murine livers.

A, Schematic of Cre-expression patterns from Albumin-Cre and Zone-specific Cre driver alleles. CV: central vein. **B**, Representative immunofluorescent images of hepatic HA-GFP-OMP25 expression in the indicated Cre-driver mice. HA (green), DAPI (blue). Scale bar, 100 μm. **C**, Schematic of rapid liver mitochondrial isolation. 70% PHx was performed 7 days after a single tamoxifen injection (Day 0). Samples were collected at Day 0 and Day 2 post PHx, and HA-labelled mitochondria were rapidly pulled down using anti-HA beads. **D**, Heatmap (z-score values) for 173 detected mitochondrial metabolites from Alb-Cre; LSL-HA-eGFP-OMP25 liver mitochondria at Day 0 (black) and Day 2 (red) post PHx. **E**, Principal components analysis of the metabolomes from total hepatocyte mitochondria at Day 0 and 2 post PHx. The percentages of total variance of principal components 1 and 2 (PC1 and PC2) are indicated on the x and y axes. **F**, Relative abundance of the indicated

metabolites from total hepatocyte mitochondria. *n*=5 per group. nd, not detected. Same color scheme as E. **G**, Principal components analysis of the mitochondrial metabolomes from Zone 1, 2, or 3 hepatocyte mitochondria at Days 0 and 2 post PHx. The percentages of total variance of principal components 1 and 2 (PC1 and PC2) are indicated on the x and y axes. **H**, Relative abundance of the indicated metabolites from zone 1, 2, or 3 hepatocyte mitochondria at Day 0 and Day 2 post PHx. *n*=5 mice per group. nd, not detected. Same color scheme as G. Statistical significance was assessed using Welch's *t*-test (F,H), with corrections for multiple comparisons. Dot and whisker plots indicate median values and interquartile ranges. Ovals indicate 95% confidence intervals. The number of biological replicates in each group and false discovery rates (q value) are indicated in the figure or above.

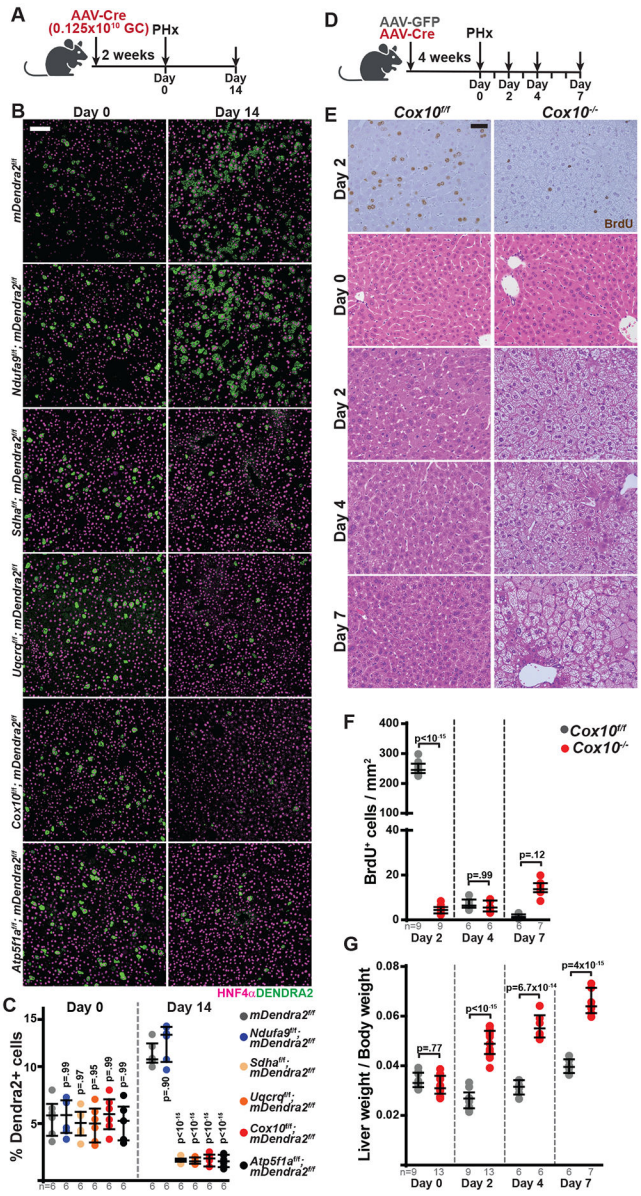

Figure 2. The mitochondrial ETC is required for liver regeneration.

A, Schematic of experiment of low-dose AAV tracing protocol. 70% PHx was performed 14 days after AAV-Cre ($0.125x10^{10}$ genome copies (GC) per mouse) administration. Samples were harvested 14 days later, and assessed for DENDRA2 expression. **B**, Representative immunofluorescent images of indicated livers at Day 0 and Day 14 post PHx. Scale bar, 100 μm. **C**, Quantitation of DENDRA2$^+$ cells (as a percentage of HNF4α$^+$ cells) in livers of the indicated mice. p values reflect comparisons with the control (*mDendra2$^{f/f}$*) group for each timepoint. **D**, Schematic of experiment of high-dose AAV protocol. 70% PHx (Day 0) was performed 28 days after AAV-Cre and AAV-GFP ($5x10^{10}$ GC per mouse) injection. Livers were harvested and analyzed at various time points post PHx. **E**, Representative BrdU immunohistochemistry and H&E images of indicated mice at the indicated timepoints post PHx. Scale bar, 50 μm. **F**, Quantitation of BrdU$^+$ cell numbers (normalized to liver area)

of indicated mice at various timepoints post PHx. **G**, Liver/body weight ratio of indicated mice at various time points post PHx. Same color scheme as F. Statistical significance was assessed using two-way ANOVA with adjustments for multiple comparisons (C,F,G). Dot and whisker plots indicate median values and interquartile ranges. The number of biological replicates in each group and p values are indicated in the figure.

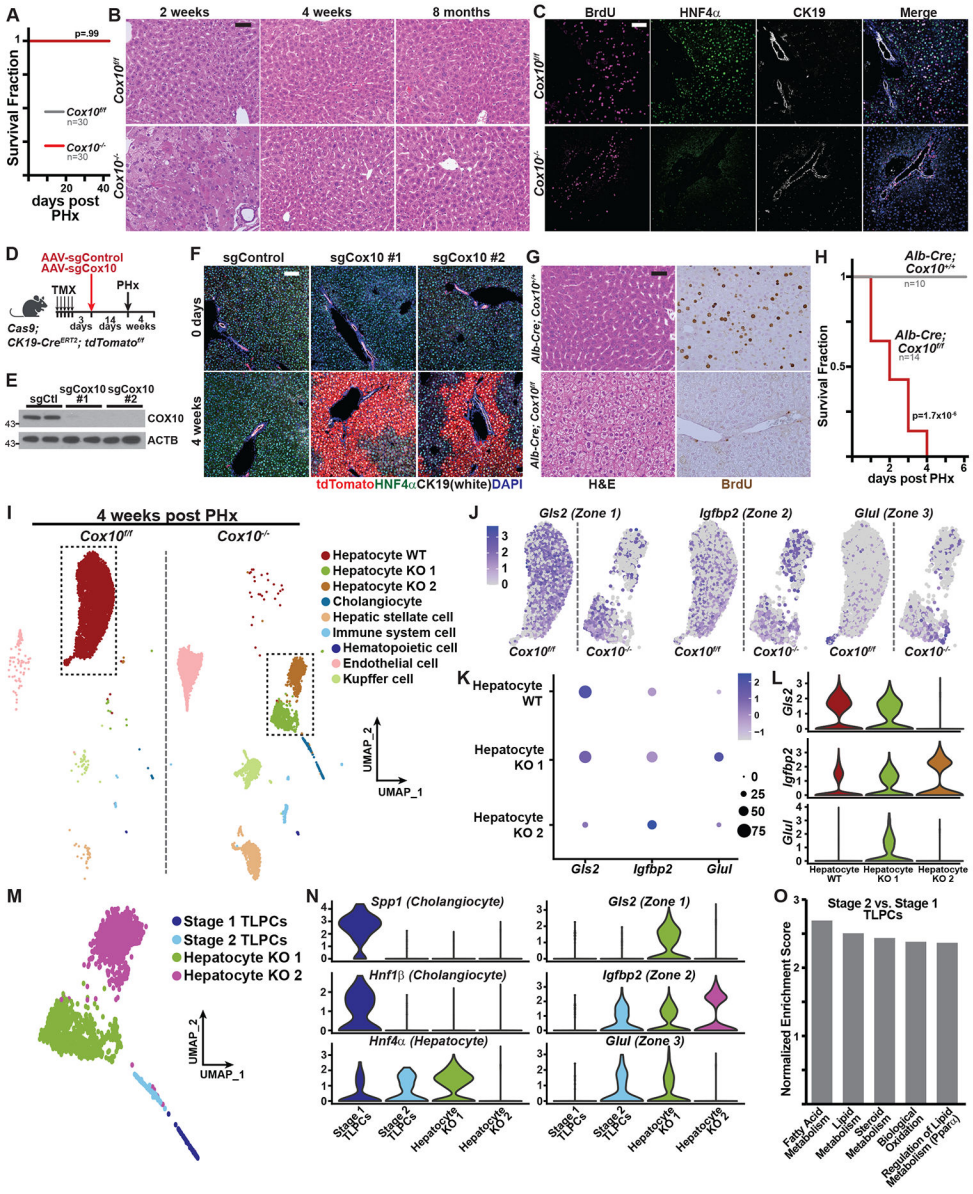

Figure 3. Transdifferentiation of biliary epithelial cells is stimulated after mitochondrial complex IV inhibition in hepatocytes.

A, Survival fraction of *Cox10*$^{f/f}$ and *Cox10*$^{-/-}$ mice post PHx. **B**, Representative H&E liver images at timepoints post PHx. Scale bar, 50 μm. **C**, Representative immunofluorescent liver images at 2 days post PHx. Scale bar, 100 μm. **D**, Protocol for cholangiocyte lineage tracing: AAV-sgControl or AAV-sgCox10 were administered to tamoxifen-treated *CK19-Cre*^{ERT2}*; Rosa26-tdTomato; Rosa26-Cas9* mice. A 70% PHx was performed 14 days later, and livers were analyzed 4 weeks post PHx. **E**, Western blot analysis of liver lysates 14 days after AAV injection. ACTB levels are shown as a loading control. Molecular weight markers are indicated in kilodaltons. **F**, Representative immunofluorescent images of livers at timepoints post PHx. Scale bar, 100 μm. **G**, Representative H&E and BrdU immunohistochemistry of livers at 2 days post PHx. Scale bar, 50 μm. **H**, Survival fraction of *Alb-Cre; Cox10*$^{f/f}$ and *Alb-Cre; Cox10*$^{+/+}$ mice post PHx. **I**, UMAP visualization from snRNA sequencing in

Cox10$^{f/f}$ and *Cox10*$^{-/-}$ livers at 4 weeks post PHx. **J**, UMAP plots showing expression of *Gls2*, *Igfbp2*, and *Glul* in hepatocyte clusters. **K**, Dot plot showing relative expression of the indicated genes in hepatocyte clusters. Dot size indicates the percentage of cells expressing each gene, and color indicates average mRNA level. **L**, Violin plots for expression of the indicated genes in hepatocyte clusters. **M**, UMAP visualization of hepatocyte and cholangiocyte clusters from *Cox10*$^{-/-}$ liver. **N**, Violin plots for expression of the indicated genes in hepatocyte and cholangiocyte clusters of *Cox10*$^{-/-}$ liver. **O**, Top 5 upregulated pathways in GSEA of stage 2 vs. stage 1 TLPCs of *Cox10*$^{-/-}$ liver. Statistical significance was assessed using a log-rank test (A and H). The number of biological replicates in each group and p values are indicated in the figure.

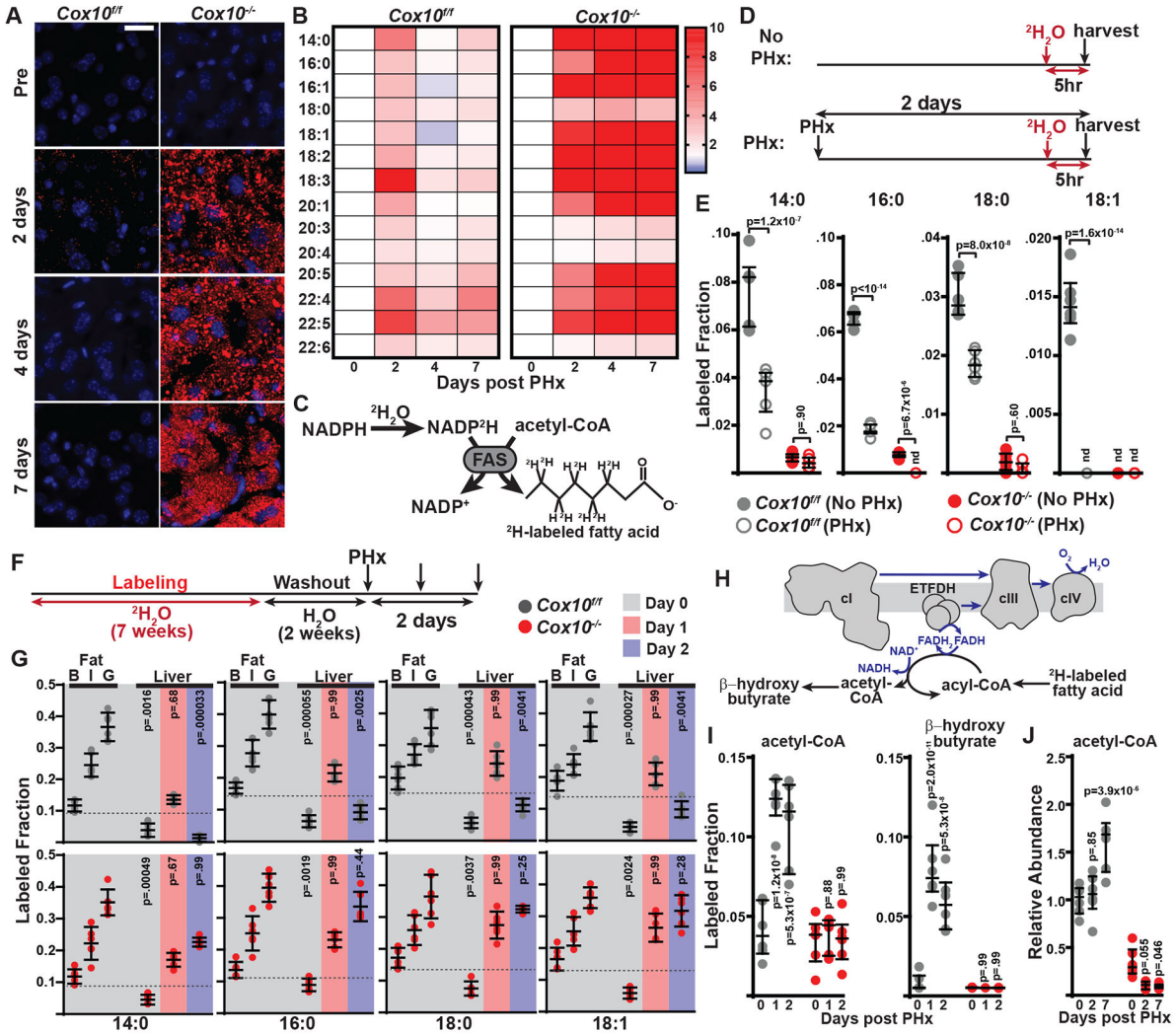

Figure 4. Hepatic oxidation of peripheral fatty acids is stimulated during liver regeneration.

A, Representative immunofluorescent images of liver Nile Red staining at the indicated timepoints post PHx. Nile Red (red), DAPI (blue). Scale bar, 20 μm. **B**, Heatmap (*z*-score values) of the indicated fatty acid species abundances in livers at various time points post PHx. **C**, Schematic of expected labeling of fatty acids with $^{2}H_2O$ administration. FAS, Fatty acid synthase. **D**, Experimental protocol for short-term $^{2}H_2O$ labeling: At 5 hours before liver collection, a single dose of $^{2}H_2O$ was administered to mice. **E**, Total labeled fraction of indicated liver fatty acid species by short-term (5 hours) $^{2}H_2O$ tracing (from D) in the indicated genotypes. **F**, Schematic of long-term (7 weeks) $^{2}H_2O$ labeling experiment to evaluate fate of peripheral fatty acids. **G**, Total labeled fraction of indicated fatty acid species by long-term $^{2}H_2O$ tracing in liver and different adipose tissues at the indicated time points post PHx. p values reflect comparison with the labeling in fat pads for that species and genotype on Day 0. B, brown fat. I, inguinal fat pad. G, gonadal fat pad. **H**, Schematic of mitochondrial fatty acid oxidation to produce acetyl-CoA and β-hydroxybutyrate. **I**, Total labeled fraction of liver acetyl-CoA and β-hydroxybutyrate from long-term $^{2}H_2O$ tracing (from F) at the indicated time points post PHx. p values reflect comparison with the Day 0

group for each genotype. **J**, Relative abundance of acetyl-CoA in livers at the indicated time points post PHx. p values reflect comparison with the day 0 group for each genotype. The same color scheme is used throughout. Statistical significance was assessed using two-way ANOVA (E, I, J), or Kruskal-Wallis (G) tests with adjustments for multiple comparisons. Dot and whisker plots indicate median values and interquartile ranges. n=6 mice in each group were used in B, E, G, I, J. p values are indicated in the figure.

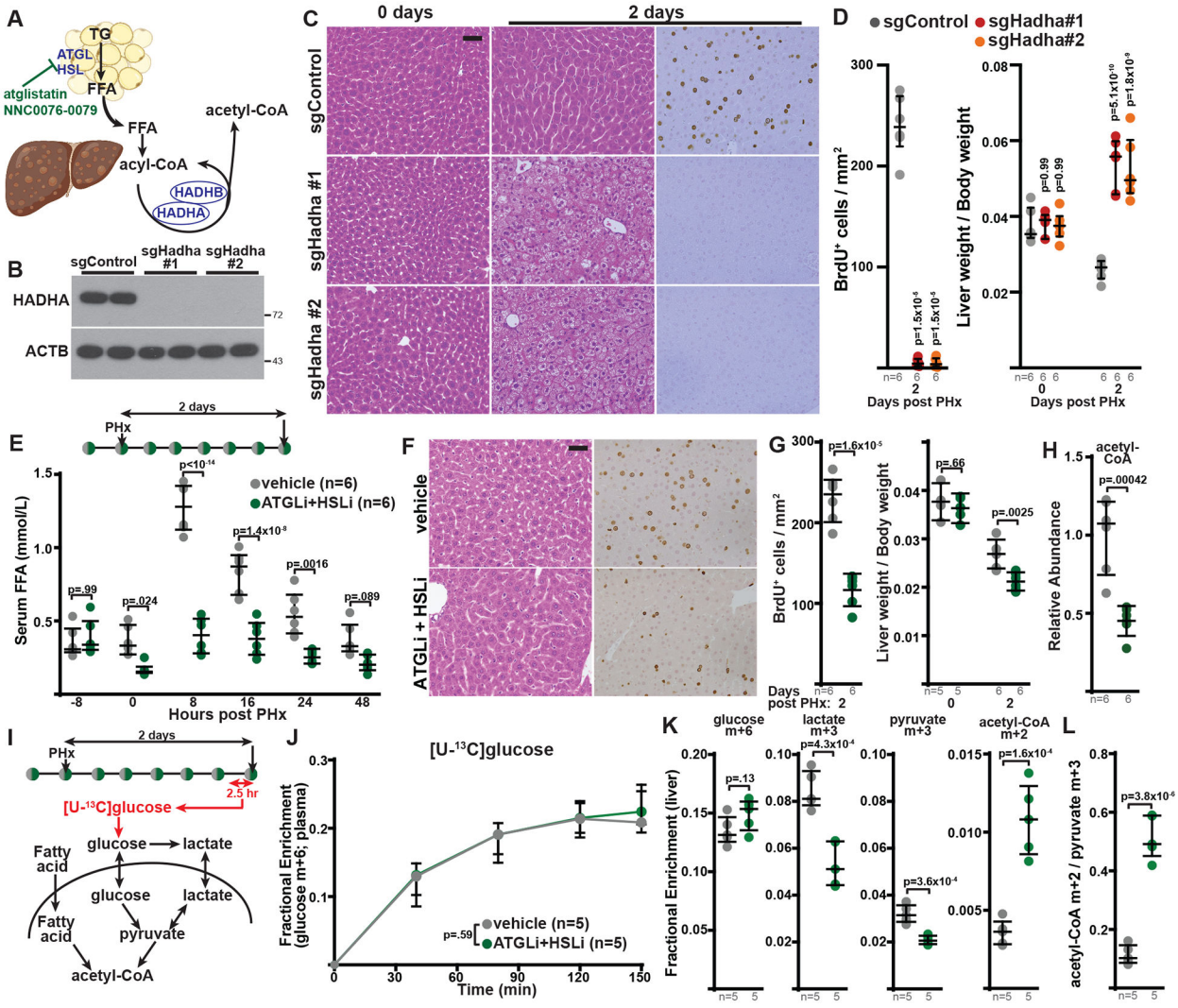

Figure 5. Peripheral fatty acid mobilization promotes hepatocyte proliferation.

A, Schematic of free fatty acid (FFA) mobilization from adipose tissue to liver to produce acetyl-CoA via mitochondrial fatty acid oxidation. ATGL, HSL inhibitors are indicated (green). **B**, Western blots for HADHA levels in livers from sgRNA-treated mice. ACTB levels are shown as a loading control; molecular weight markers are in kilodaltons. **C**, Liver H&E and BrdU immunohistochemistry at 2 days post PHx. Scale bar, 50 μm. **D**, $BrdU^+$ cell numbers (per liver area) and liver/body weight ratios. p values reflect comparison with sgControl group for each timepoint. **E**, (Top) Protocol for lipolysis inhibitor administration: Vehicle or inhibitors were administered to C57BL/6J mice every 8 hours during PHx. (Bottom) Serum FFA concentrations at the indicated timepoints. **F**, Liver H&E and BrdU immunohistochemistry of treated C57BL/6J mice at 2 days post PHX. Scale bar, 50 μm. **G**, $BrdU^+$ cell numbers (per liver area) and liver/body weight ratio in treated C57BL/6J mice. **H**, Relative abundance of liver acetyl-CoA in treated C57BL/6J mice at 2 days post PHx. Same color scheme as E. **I**, Protocol for [U-^{13}C]glucose tracing post PHx. **J**, Labeled fraction of plasma glucose m+6 in treated C57BL/6J during [U-^{13}C]glucose infusions. **K**, Fractional enrichment of the indicated isotopologues in livers of treated C57BL/6J mice

following [U-^{13}C]glucose infusion at 2 days post PHx. **L**, Liver acetyl-CoA m+2/pyruvate m+3 ratio in treated C57BL/6J mice following [U-^{13}C]glucose infusion at 2 days post PHx. Same color scheme as J. Statistical significance was assessed using Brown-Forsythe ANOVA (BrdU in D), or two-way ANOVA (D, G, E and J), or Student's t-test for (BrdU in G, H,K,L) with adjustments for multiple comparisons. Dot and whisker plots indicate median values and interquartile ranges. The number of biological replicates in each group and p values are indicated in the figure.

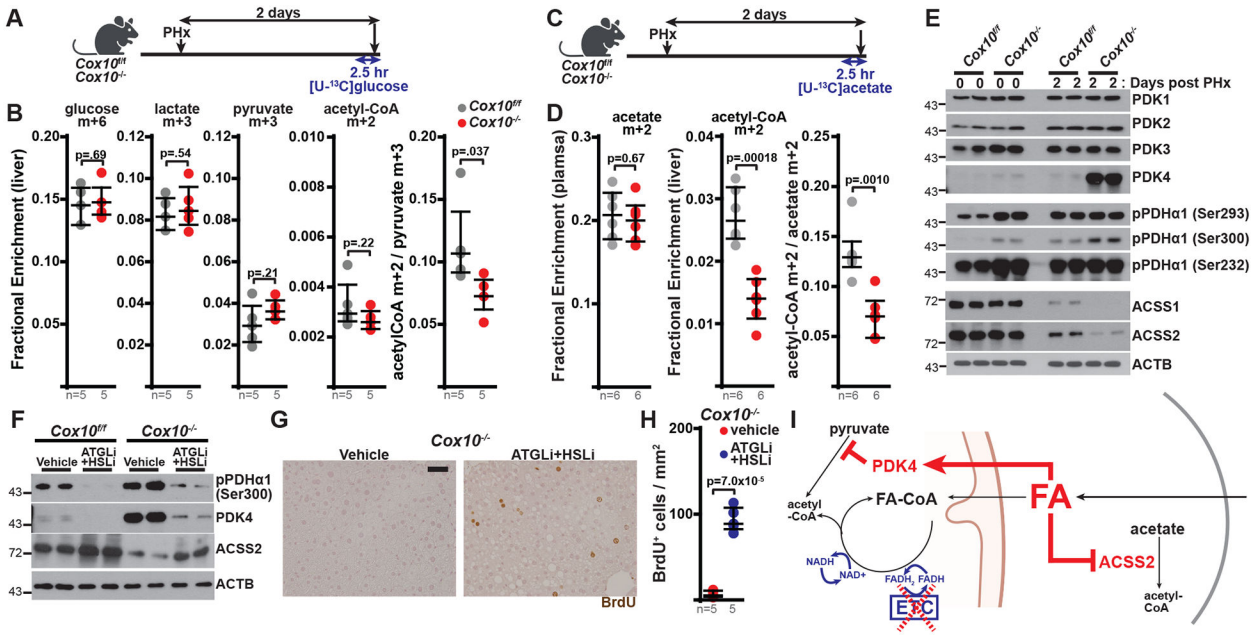

Figure 6. Fatty acid accumulation inhibits acetyl-CoA production.

A, Schematic of [U-^{13}C]glucose tracing in *Cox10*$^{f/f}$ and *Cox10*$^{-/-}$ mice during liver regeneration. **B**, Fractional enrichment of the indicated isotopologues following [U-^{13}C] glucose infusion at 2 days post PHx. **C,** Schematic of [U-^{13}C]acetate tracing in *Cox10*$^{f/f}$ and *Cox10*$^{-/-}$ mice during liver regeneration. **D**, Fractional enrichment of the indicated isotopologues following [U-^{13}C]acetate infusion at 2 days post PHx. **E**, Western blot analysis in *Cox10*$^{f/f}$ and *Cox10*$^{-/-}$ liver protein lysates at the indicated time points post PHx. ACTB levels are shown as a loading control. **F**, Western blot analysis in liver protein lysates from animals treated with vehicle or ATGL and HSL inhibitors. ACTB levels are shown as a loading control. **G,** Representative BrdU immunohistochemistry images of *Cox10*$^{-/-}$ mice treated with vehicle or lipolysis inhibitors at 2 days post PHx. Scale bar, 50 μm. **H**, BrdU^{+} cell numbers (normalized to liver area) in the indicated mice. **I,** Proposed model: In the setting of ETC dysfunction, fatty acid (FA) buildup in hepatocytes inhibits acetyl-CoA production via the induction of PDK4 and suppression of ACSS2 expression. Statistical significance was assessed using Student's t-test (B,D) or Welch's t-test (H). Dot and whisker plots indicate median values and interquartile ranges. The number of biological replicates in each groups and p values are indicated in the figure. Molecular weight markers are indicated in kilodaltons.

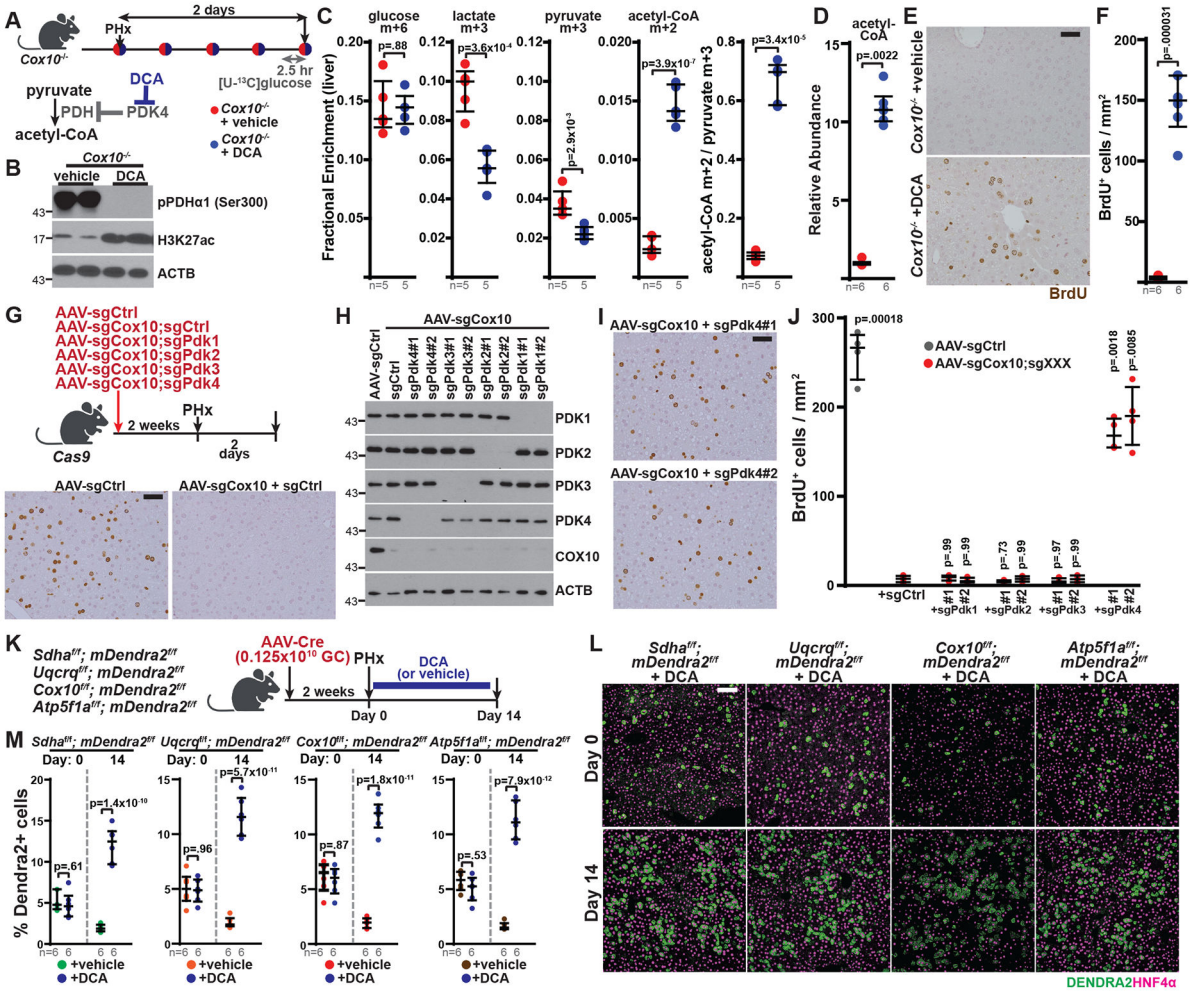

Figure 7. PDK4 inhibition promotes expansion of hepatocytes with ETC dysfunction.

A, Schematic of DCA treatment in *Cox10*$^{-/-}$ mice (top), and PDK4-PDH pathway inhibition by DCA (bottom). **B,** Western blots from livers of treated *Cox10*$^{-/-}$ mice at 2 days post PHx. ACTB levels are shown as a loading control. **C**, Fractional enrichment of the indicated liver isotopologues in treated *Cox10*$^{-/-}$ mice (following [U-^{13}C]glucose infusion at 2 days post PHx). **D**, Relative abundance of liver acetyl-CoA from treated *Cox10*$^{-/-}$ mice at 2 days post PHx. Same color scheme as A. **E**, Liver BrdU immunohistochemistry images at 2 days post PHx. Scale bar, 50 μm. **F**, BrdU^{+} cell numbers (per liver area) of *Cox10*$^{-/-}$ livers at 2 days post PHx. Same color scheme as A. **G**, (Top) Schematic of simultaneous deletion of *Cox10* and *Pdk* family members. (Bottom) Liver BrdU immunohistochemistry from *Cas9* mice administered the indicated AAVs. Scale bar, 50 μm. **H**, Western blots from liver of *Cas9* mice administered the indicated AAVs. ACTB is shown as a loading control. **I**, Liver BrdU immunohistochemistry from mice administered the indicated AAVs. Scale bar, 50 μm. **J**, BrdU^{+} cell numbers (per liver area) at 2 days post PHx. n=4 mice per group. **K**, Schematic for DCA treatment in animals with mosaic livers induced by low titer AAV. **L**, Liver immunofluorescent images from DCA-treated mice at the indicate timepoints post PHx. Scale bar, 100 μm. **M**, Quantitation of DENDRA2^{+} cells (as a percentage of HNF4α^{+} cells) in livers at Day 0 and 14 post PHx. Statistical significance was assessed

using Student's t-test (C), Welch's t-test (C,F), or Mann-Whitney (D), Brown-Forsythe (J), or two-way ANOVA (M) tests with adjustments for multiple comparisons. Dot and whisker plots indicate median values and interquartile ranges. The number of biological replicates in each groups and p values are indicated above or in the figure. Molecular weight markers are indicated in kilodaltons.